Focal shift induced by source displacements and optical figure errors[1]

Michele Manfredda,[a]* Lorenzo Raimondi,[a] Nicola Mahne[b] and Marco Zangrando[a,b]

[a]Elettra-Sincrotrone Trieste SCpA, SS 14 – km 163.5, 34149 Basovizza, Trieste Italy, and [b]Istituto Officina dei Materiali – CNR, SS 14 – km 163.5, 34149 Basovizza, Trieste Italy. *Correspondence e-mail: michele.manfredda@elettra.eu

In this work the longitudinal shifts of the focal plane of an ellipsoidal mirror induced by longitudinal shifts of the source and by the optical figure error of the mirror itself are investigated. The case of an ideal mirror illuminated by a Gaussian beam is considered first, deriving an analytical formula predicting the source-to-focus shift. Then the realistic case of a mirror affected by surface shape defects is examined, by taking into account metrological data and numerically solving the Huygens–Fresnel integral. The analytical and numerical solutions in the ideal and real cases are compared. Finally, it is shown that an additional dependence of the focal shift is introduced on the wavelength and the pointing angle of the source. Both effects are investigated by numerical computations. We limit the treatment in the XUV spectral range, choosing as a test bench the Kirkpatrick–Baez mirror system of the DiProI and LDM end-stations and at the FERMI seeded free-electron laser (FEL). The work is primarily aimed at disentangling the different causes of focal shift at FEL light sources, where source position, wavelength and pointing angle are either tunable or rapidly fluctuating. The method can be easily extended to parabolic reflectors and refractors (lenses) with other kinds of illuminating sources and wavelengths.

1. Introduction

Ellipsoidal or elliptical mirrors are popular focusing elements at X-ray wavelengths (Nightingale, 1993; Citterio & O'Dell, 2004). They are used both for imaging, like in astronomical telescopes, and for concentrating high-energy flux into a micrometre or sub-micrometre spot size, like in synchrotrons or free-electron lasers (FELs) (Kim *et al.*, 2017). For these reasons, their performance has been thoroughly studied, with a particular emphasis on the causes that reduce their focusing (or imaging) sharpness. These causes typically include the surface shape accuracy and the surface finishing. Since they represents a crucial element in mirror manufacturing, different authors have tackled the idea of using the surface metrology to predict, by means of different approaches, the so-called point spread function, which provides a quantification of the smallest achievable spot size (or equivalently of the best image resolution) (Takacs, 1986; Willingale, 1988; O'Dell *et al.*, 1993; Aschenbach, 2005; Raimondi & Spiga, 2015).

In this work, we intend to put the accent on a different aspect, *i.e.* the shift of the focal plane along the propagation direction and its possible causes.

The original motivation lies in the recent spread of the use of elliptical mirrors across FEL facilities. These light sources are distinguished from synchrotrons, the other high-performance terrestrial X-ray sources, not only for their unique radiation properties (laser-like coherence and ultra high-bril-

Horizontal K-B mirror
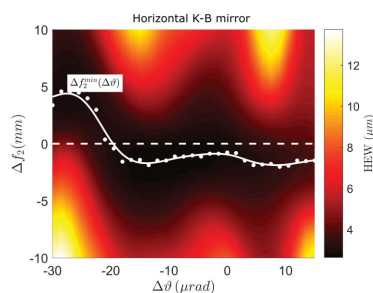
liance) but also for the mechanism used to extract radiation from the electron beam. In particular, coherent emission from FELs relies on an instability that develops on the electron beam when passing through a long undulator. Due to this emission mechanism, important parameters such as the effective source position and dimension may not be known *a priori* (Bachelard *et al.*, 2011), as they depend on the particular machine configuration required for optimizing the lasing process. The longitudinal source position, for instance, may suffer large r.m.s. fluctuations, of the order of $\sim$7–10 m (Kayser *et al.*, 2016; Liu *et al.*, 2018). In some cases, it can be even adjusted to meet the experiment needs: for instance, in the case when the FEL undulating length is split into different sections to accommodate the request of a multicolor FEL (Allaria *et al.*, 2013; Hara *et al.*, 2013; Lutman *et al.*, 2016; Ferrari *et al.*, 2016; Prince *et al.*, 2016), or when different sections are tuned to emit at a distinct polarization (Allaria *et al.*, 2014; Ferrari *et al.*, 2015). The scenario is really complex, since both the source metrology and the focusing optics play a role, and the shift of the focal plane is determined by the interplay between the two. In particular, the demagnification ratios at play are very large ($1/M \simeq 1/50\times$ to $1/100\times$), so that a small shift of the source translates into a large shift of the focal spot at the end-station.

The longitudinal position of the source, however, is not the sole responsibility of the shift of the focal plane. In the presence of optics affected by surface error defects, there are other parameters that may induce a focal shift. The most representative ones are the wavelength of the source and its angular pointing. Their importance lies in the fact that FELs are machines with high wavelength tunability, and with characteristic shot-to-shot jitter of the electron orbit, which ultimately transfers to the wavevector of the photon beam. Both phenomena induce an additional shift of the focal plane that is not connected with the longitudinal position of the source, and which therefore needs a dedicated investigation.

In this perspective, the first aim of this work is to investigate the longitudinal shifts of the focal spot of an ellipsoidal mirror induced by longitudinal shifts of the source. In doing so, we will first consider the simple case of an ideal mirror, deriving an analytical formula predicting the source-to-focus shift. Then we will examine the realistic case of a mirror affected by surface defects, by numerically solving the Huygens–Fresnel integral. We will compare the analytical and numerical solution, both in the ideal and real cases. Finally, we will investigate the dependence of the focal shift on the wavelength and the pointing angle. This will be done by means of numerical simulations, since the effects are intimately connected to the surface defects and require metrological data to be taken into account. We will limit the treatment to the XUV spectral range, choosing as a test bench the Kirkpatrick–Baez (K–B) mirror system of the DiProI and LDM beamlines (Pedersoli *et al.*, 2011; Capotondi *et al.*, 2015; Svetina *et al.*, 2015) at the FERMI FEL (Allaria *et al.*, 2015). It is interesting to remark that FERMI operates in the so-called 'seeded' configuration (Prazeres *et al.*, 1988; Doyuran *et al.*, 2001), where the initial instability is triggered by a high-power conventional laser. As

a consequence, the final emitted light has a high degree of spectral purity, and it can be likened to a $\mathrm{TEM_{00}}$ Gaussian mode (Allaria *et al.*, 2012). For this reason, in the following we will use the Gaussian source over the conventional point source emitting spherical waves, since the diffraction of a Gaussian beam focused through an elliptical mirror causes, in general, an extra focal shift, as we will see in the next section.

2. Focusing a Gaussian beam through an ideal elliptical section

2.1. Analytical derivation

The focusing of a spherical Gaussian beam through a thin lens has been extensively investigated by Siegman & Weichel (1974) and Self (1983) in a geometrical optics approach. Focusing upon conical reflecting surfaces has been treated in many possible configurations, including reflection and refraction at tilted ellipsoidal surfaces (Massey & Siegman, 1969; Yu & Dou, 2010), reflection on paraboloid and hyperboloid interfaces (Abadi *et al.*, 2015; Gangopadhyay & Sarkar, 1997) and the effects of distortions on Gaussian beams upon elliptical mirrors. However, none of these works present in a simple form the results we are interested in, *i.e.* providing the relation between the longitudinal source shift and the corresponding focal shift of a Gaussian beam focused by an elliptical mirror.

The situation of interest is illustrated in Fig. 1: a curved off-axis elliptical profile is used to focus a Gaussian source which is ideally located at the focal point F_1 of the ellipse. With respect to cylindrical coordinates (z_1, r) with the origin at F_1, the intensity distribution of a propagated Gaussian beam normalized to unit total beam power is

$$I(z_1, r) = 2/\pi w(z_1)^2 \exp\left[-2r^2/w^2(z_1)\right], \quad (1)$$

where w_0 is the beam radius at the waist ($z_1 = 0$), $z_\mathrm{R} \equiv \pi w_0^2/\lambda$ is the Rayleigh length, and $w(z_1) = w_0[1 + (z_1/z_\mathrm{R})^2]^{1/2}$ is the evolving beam size. If the mirror's material length is small with respect to the total focus-to-focus distance, the radii of curvature of the incident and reflected beams (f_1, f_2) can be treated as constants. The quantities f_1 and f_2 are thus referred to as the focal lengths of the mirror. In a FEL facility the focal point F_1 is typically set at the center of the last undulator.
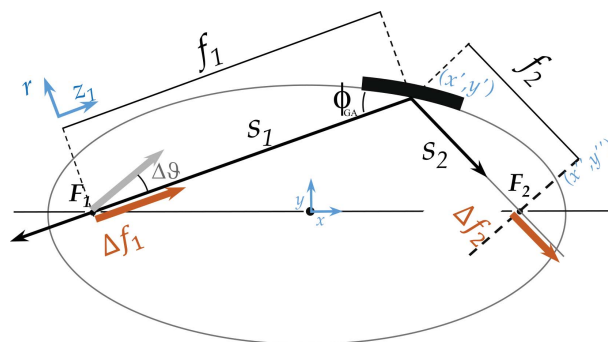

Figure 1
Geometry of an off-axis elliptical mirror.

Table 1
Parameters of the elliptical mirror and of the photon source used throughout this work.

$m_0 = f_2/f_1$ is the nominal magnification. w_0 is the beam size parameter.

	f_1	f_2	f	$1/m_0$	w_0
V	98.754	1.750	1.700	57.1	180 μm
H	99.304	1.200	1.186	82.754	

We are interested in finding the relation between the shift Δf_2 of the focal plane (around F_2) and the shift Δf_1 of the source (around F_1). The focal lengths of the vertical (V) and horizontal (H) K–Bs and the beam radius w_0 used throughout this work are reported in Table 1.

If we had a parabolic mirror (or a thin lens) of focal length f, the solution would be expressed by the lens-maker equation for a Gaussian beam (Self, 1983),

$$\frac{s_2}{f} = 1 + \left(\frac{s_1}{f} - 1\right) m^2(z_R, s_1, f). \qquad (2)$$

Here s_1 and s_2 are the source-to-lens and the lens-to-image distances, oriented as in Fig. 1, and $m(z_R, s_1, f)$ is the Rayleigh length-dependent magnification, defined as

$$m(z_R, s_1, f) = \frac{1}{\left[(s_1/f - 1)^2 + (z_R/f)^2\right]^{1/2}}. \qquad (3)$$

Equation (2) is similar to the ordinary lens-maker equation except for the presence of the term z_R, which discriminates between the cases of a Gaussian ($z_R > 0$) or a point-like source ($z_R = 0$). These two kinds of source have different behavior when focused, as we will see in Section 2.2.

Equation (2) can be applied to an elliptical section of focal lengths f_1, f_2 by finding the equivalent focal length f. This corresponds to approximating an elliptical reflector to a parabolic reflector, and is done by matching the incident and reflected phase front radii of curvature (f_1, f_2) at the interface. The method was first proposed in the field of ellipsoidal reflectors for antennas (Chu, 2004), and then also reported by Goldsmith (1998) and Yu & Dou (2010). The equivalent focal length of an elliptical arc can be expressed as

$$\frac{1}{f} = \frac{1}{f_1} + \frac{1}{f_2} = \frac{b^2}{4a \cos^2 \phi_{GA}}, \qquad (4)$$

where a and b are the coefficients of an ellipse written in the canonical form $x^2/a^2 + y^2/b^2 = 1$ and ϕ_{GA} is the grazing angle. Equation (4) can be regarded as the equivalent focal length of a section of the ellipse in terms of the distances to the focii, and allows us to treat an elliptical arc section as a single-focal-length optics. The conditions for which equation (4) holds are discussed by Chu (2004), and they involve considerations on the symmetry of the mirror (related to the f_1/f_2 ratio) and on the incidence angles used. Without entering the details, since in our setup the material length of the mirror L is very small compared with the major axis of the ellipse ($L/2a \simeq 2 \times 10^{-2}$), it turns out that proper conditions are met. A simulation

confirming the validity of the underlying assumption will be shown in Section 3.3.

In order to find the relation mapping the source shift into the focal shift, it is useful to define $\Delta f_1 = s_1 - f_1$ and $\Delta f_2 = s_2 - f_2$ (where f_1 and f_2 are constants) which, substituted into equation (2), yields

$$\Delta f_2(\Delta f_1; s_1, f, z_R) = m^2(\Delta f_1, f, z_R)\, \Delta f_1. \qquad (5)$$

When considering a beam of fixed waist radius w_0, it may be convenient to replace z_R in equation (5). Before discussing equation (5), we will consider the Gaussian nature of the source.

2.2. Focal shift due to source Gaussianity

Equations (2) and (4) set an analogy between a thin lens and an elliptical-arc section when they are illuminated either by a Gaussian beam or by a uniform spherical wave.

The most striking difference between a spherical wave and a Gaussian beam is that, while the first one placed at the front-focal plane of a positive lens yields a collimated beam [Fig. 2(a)], a Gaussian waist yields an emerging beam with a waist at the back-focal plane [Fig. 2(e)]. Such a behavior is shown in Fig. 2, where equation (2) is shown in graphical form for different values of z_R/f. If $z_R = 0$ (point source), then equation (3) has a singularity for $s_1 \to f$, which generates the branches of a hyperbola of Fig. 2 (left). This corresponds to having a collimated beam, as predicted by geometrical optics. Conversely, if $z_R/f > 0$ (Gaussian source), the singularity is removed and all the curves pass through the point $s_1/f = s_2/f = 1$. This corresponds to the simultaneous existence of a waist in the front and back focal planes ($s_1 = s_2 = f$).

By introducing the equivalent focal length f, the behavior of an elliptic section can be described in the same way: a point source set at the focal point F (corresponding to the effective focal length f) is imaged into a collimated beam [Fig. 2(c)]. Such a configuration is of little interest for an elliptical mirror, since collimating can be better achieved by means of pure parabolic profiles. In its usual operating condition, an elliptical arc section focuses a point source at F_1 into F_2 [Fig. 2(d)]. This case can be likened to a source placed off the focal point of a lens [Fig. 2(b)].

If we now consider a Gaussian source, then the waist at the front focal point F_1 is no longer focused at F_2 but at a shorter distance $f < s_2 < f_2$ [Figs. 2(h) and 2(f)]. For a beam of fixed waist parameter w_0, the Gaussian-induced focal shift strongly depends both on the wavelength [Fig. 3(a)] and on the ratio $f_1:f_2$ [inset of Fig. 2(d)], according to equations (2) and (4). Using the parameters of Table 1, the focal shift is negligible at large wavelengths ($\Delta f_2 \lesssim 100$ μm for $\lambda > 40$ nm) while it becomes progressively appreciable at shorter wavelengths ($\Delta f_2 \simeq 2$ mm at $\lambda = 4$ nm). In evaluating $\Delta f_2(\lambda; s_1, f)$ it is stressed that the source is meant to be at F_1 ($\Delta f_1 = 0$), and thus the existence of a focal shift is solely due to the Gaussian nature of the source. Although in principle it would provide an indirect way of measuring the source waist size, it will be clear from the following sections that the presence of defects in
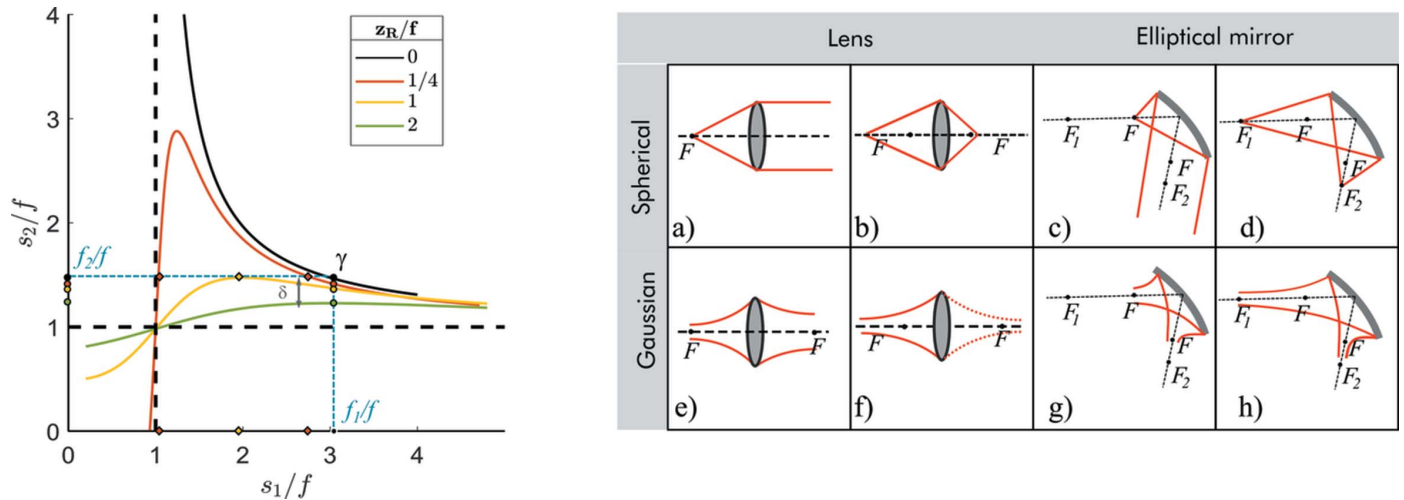
Figure 2
Left pane: Cartesian plot of the lens formula for Gaussian beams showing the normalized source distance s_1/f versus the normalized image distance s_2/f, with normalized Rayleigh length of the input beam z_R/f as parameter. Dashed blue line: behavior of a hypothetical elliptical mirror with focal lengths f_1/f, f_2/f. The source lying at f_1/f is imaged to a distance $s_2/f < f_2/f$ depending on the Rayleigh length z_R/f of the source, with a single image for each value of z_R/f. The source lying at f_2/f is imaged to a distance $s_1/f < f_1/f$ with a number of solutions depending on the value z_R/f. For a given couple of values (f_2/f, z_R/f), there is a minimum distance $s_2/f < \delta$ beyond which no real image is produced. Right pane: comparison of a thin lens and elliptical mirror when illuminated by a spherical wave (upper row) and a Gaussian wave (lower row). F_1, F_2, F mark the points corresponding to the focal lengths f_1, f_2, f, respectively [equation (4)]. (a, c) Collimating a point source to a plane wave. (e, g) Waist-to-waist imaging. (b, d) Extrafocus-to-intrafocus imaging. In an elliptical mirror (c), the relevant extrafocal/intrafocal points are the focii F_1, F_2. (f, h) The same as before but with a Gaussian beam. In an elliptical mirror (h), the waist at F_1 is imaged into an intermediate position between F and F_2.
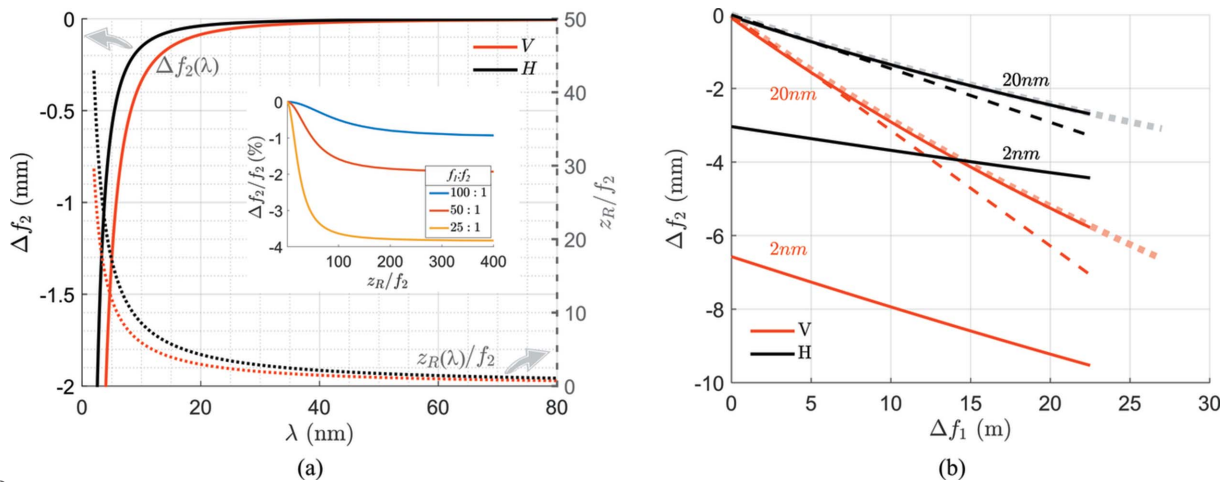

Figure 3
(a) Solid lines: focal shift as a function of wavelength according to equation (5) (left axis). Dotted lines: normalized Rayleigh length as a function of wavelength (right axis). Inset: relative focal shift as a function of normalized Rayleigh length for distinct values of demagnification (see legend). The source lies at F_1 ($\Delta f_1 = 0$). (b) Focal shift for K–B mirrors as a function of the source shift at $\lambda = 2, 20$ nm. Solid line: graph of $\Delta f_2(\Delta f_1)$ from equation (5). Thick dashed line: graph of $\Delta f_2(\Delta f_1)$ from equation (5) with $z_R = 0$. Thin dashed line: graph of $\Delta f_2(\Delta f_1)$ from equation (6) (nominal magnification).

the mirror surface largely alters the fashion of the curve in Fig. 3(b).

2.3. Focal shift due to source shift

Equation (5) is shown in graphical form in Fig. 3 for $\lambda = 20$ nm and $\lambda = 2$ nm (solid curves). They can be regarded as the non-normalized version of the curves of Fig. 2 taken for very high values of s_1/f. Specifically, the range of s_1/f is about $f_{1V}/f_V \simeq 57$ for the vertical K–B and about $f_{1H}/f_H \simeq 83$ for the horizontal K–B, with $1/f_V \equiv 1/f_{1V} + 1/f_{2V}$ and $1/f_H \equiv 1/f_{1H} + 1/f_{2H}$. The evaluated function $\Delta f_2(\Delta f_1)$ exhibits just a very

mild convexity and can be approximated to a straight line whose slope and zero-intercept are essentially determined by the $(z_R)^2$ parameter in the function $m(s_1, f, z_R)$. A detailed plot of the magnification can be found, for example, in the work of Self (1983). The dashed thick curves correspond to the geometrical limit of equation (3) obtained for $z_R = 0$, corresponding to the branch of hyperbole of Fig. 2. In this case the dependence on the wavelength has been dropped. The dashed thin lines are obtained by setting both $z_R = 0$ and $\Delta f_1 = 0$ in equation (3), maintaining the dependence on Δf_1 in equation (5). This corresponds to evaluating equation (5) using the constant magnification value $m_0 = f_2/f_1$, i.e. the nominal

magnification of the elliptical mirror. From the plot it turns out that, for small source shifts and within the geometric limit, the focal shift can be approximated to a line of the form

$$\Delta f_2 = m_0^2 \Delta f_1. \qquad (6)$$

We conclude this section by saying that the aforementioned results can be easily extended to the case of a possibly highly non-Gaussian beam simply by introducing the so-called 'beam propagation factor' M^2 (Siegman, 1998). This can be done by replacing z_R with z_R/M^2 in the expressions of equations (1) and (2).

3. Focal shift induced by the figure error

3.1. Numerical computing

If the mirror profile departs from its ideal shape, then the focal shift cannot be expressed in a closed form and it shall be numerically computed by numerical evaluation of the Huygens–Fresnel integral. In doing so we make use of WISEr, a physical optics simulation package that we have developed for beamline design and the investigation of X-ray optics performance. Originally conceived for simulating X-ray tele-scopes, it has recently been included in the Orange Synchro-tron Suite (OASYS) (Sanchez del Rio & Rebuffi, 2019; Manfredda & Raimondi, 2018). In simulating the diffraction effects from ellipsoidal mirrors we follow the prescriptions of Raimondi & Spiga (2015). At grazing incidence, the influence of transverse surface errors is negligible compared with longitudinal ones (Peatman, 1997). The reflection upon a surface can be simplified to a one-dimensional problem by limiting it to the tangential defects only. The surface integral reduces to one dimension in the form

$$\mathbf{E}(x'', y'') = \int \mathbf{E}_0(x', y') \qquad (7)$$
$$\times \exp\left\{ ik\left[(x'' - x')^2 + (y'' - x'')^2\right]^{1/2}\right\} \mathrm{d}x'\, \mathrm{d}y',$$

where, referring to Fig. 1, (x'', y'') are the coordinates on the (one-dimensional) detector, (x', y') are the points on the mirror profile, and $\mathbf{E}_0$ is the complex Gaussian field evaluated on the mirror.

The new focus of the outcoming (aberrated) wavefront is found by minimizing the spot size along the longitudinal direction by sweeping the value of Δf_2. This operation numerically mimics the practical action of moving a screen back and forth around the nominal focus F_2. The sought position is labeled $\Delta f_2^{\min}$. The beam size is computed as the half energy width (HEW), i.e. as the width containing half of the total energy of the beam. Such a definition is generic enough to be suitable also for non-symmetric intensity distributions. The radius parameter w_0 corresponds to the HEW value $W_0 \simeq 0.68 \times 2/\sqrt{2}w_0$.

As an example, we show some computations of the HEW as a function of Δf_2. The ideal profile of the vertical K–B is used. Fig. 4(a) provides an overview on the behavior of the HEW as a function of the wavelength ($\lambda = 5, 10, 20, 35$ nm) for a source lying at the nominal focal plane F_1 ($\Delta f_1 = 0$) with the nominal emission angle ($\Delta\vartheta = 0$) (Fig. 1). The trend may recall that of the size parameter of a magnified Gaussian beam across the waist: $W(\Delta f_2) = W_0[1 + (\Delta f_2/m^2 z_R)^2]^{1/2}$. However, aperture diffraction effects introduced by the finite longitudinal mirror-size make the HEW deviate from the pure quadratic behavior. For the same reason, the HEW value at the waist is larger than its theoretical value W_0 and it grows accordingly with the wavelength.

Fig. 4(b) provides a comparison of the HEW between the the source in the nominal and in a shifted position ($\Delta f_1 = 0$, -11.25 m) combined with the cases of on-axis and off-axis emission angles ($\Delta\vartheta = 0, -10$ µrad) at $\lambda = 20$ nm. The length 11.25 m corresponds to half of the total FERMI undulator length and 10 µrad is an angular tilt which is typically encountered. Such a small tilt of the source does not induce any appreciable variation neither in minimum position nor in the value of the HEW (dashed curves overlap with solid curves). Consequently, the shift of the minimum still follows equation (5). Similar results would be obtained for positive values of $\Delta\vartheta$, provided that the pointing deviation is small enough to ensure negligible variation of the optical path with respect to the focal lengths f_1, f_2. In the next section we will
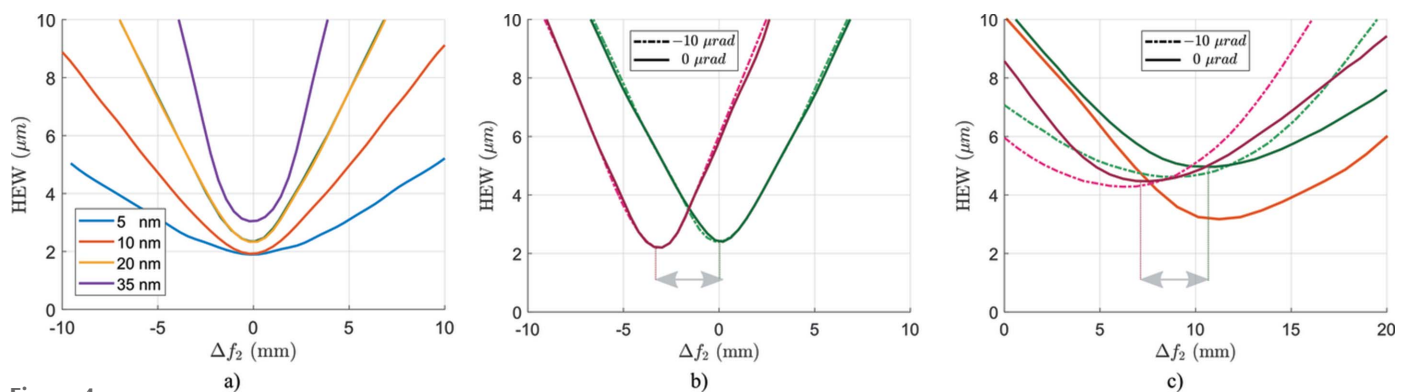

Figure 4
Simulated HEW as a function of the focus shift Δf_2 for a Gaussian source of waist radius $w_0 = 180$ µm. The vertical K–B is considered. (a) Ideal mirror profile, wavelength as input parameter (see legend). (b) Ideal mirror profile. (c) Real mirror profile. Color code for (b) and (c): green – source at $\Delta f_1 = 0$, $\lambda = 20$ nm; purple – source at $\Delta f_1 = -11.25$ m, $\lambda = 20$ nm (radiator III); orange – source at $\Delta f_1 = 0$, $\lambda = 10$ nm. Solid lines: source on-axis emission at $\Delta\vartheta = 0$. Dashed lines: source off-axis emission at $\Delta\vartheta = -10$ µrad.

see how the configuration evolves by introducing a defected mirror profile.

3.2. The figure error

The surface defects that affect a mirror are traditionally distinguished into figure error and roughness. Figure errors include medium-low spatial frequencies typically within the millimetre scale and they are measured, for example, with a long-tracing profilometer (LTP). They can be due either to the manufacturing process or, in an adaptive system, to sub-optimal bending. Roughness encompasses high spatial frequencies typically down to the micrometre scale and it is measured via phase-shift interferometry or atomic force microscopy. It is eminently due to the polishing process in manufacturing and, due to its statistical nature, it should not induce a neat curvature effect on the wavefront. For this reason it will be neglected in this work.

In Fig. 5 we show the residual height function $h(l)$, computed as the difference between the measured and the ideal curvature profiles along the longitudinal position of the mirror l (see caption for details). The measurements were performed *ex situ* with an LTP with 150 nrad angular resolution and 0.5 mm lateral resolution. The optimal curvature (measured profile) was achieved by means of iterative least-squares method (Signorato, 1999). The difference between vertical and horizontal curves, in terms of shape and peak-to-valley, is mostly due to gravitational effects: the weight of the vertical K–B mirror induces a spontaneous deformation, a catenary-like curve, which warps the quasi-elliptical desired curvature generated by the active system. On the contrary, by virtue of its orientation, the effect does not occur for the horizontal K–B [possible solutions include shape tapering (Nistea *et al.*, 2017)]. A comprehensive discussion on this kind of K–B active optical system has been given by Raimondi *et al.* (2019). The footprint of the intensity distribution that effectively illuminates the figure error varies on the divergence of the beam σ' (Fig. 5, light blue curves) which depends on the wavelength as

Figure 5
Red and black lines: figure errors of K–B mirrors (left axis). Light blue lines: normalized intensity distributions at distinct λ (right axis).

$$\sigma' = \lambda/\pi w_0. \tag{8}$$

By adding the height function $h(l)$ to the ideal curvature profile of the mirror, some major changes occur in the behavior of the HEW across the focus, in its minima and in its Rayleigh range [Figs. 4(b) and 4(c)].

First, the HEW values are higher and vary more slowly as one moves farther from the effective focal plane, resulting in an increased Rayleigh length (computed as the distance from the waist where the HEW is $\sqrt{2}$ larger). For example, considering the case $\Delta f_1 = 0$ and $\Delta \vartheta = 0$ [solid green lines in Figs. 4(b) and 4(c)], the HEW at the waist is $\sim$2.4 μm in the ideal case, while it is $\sim$5 μm in the real case. The measured Rayleigh length almost doubles as well, ranging from $\sim$2 μm (ideal case) to $\sim$5–8 μm (real case). Second, the minima of the HEWs are dramatically shifted upstream by several millimetres, which corresponds to a shift of the focal plane of the beam. The focal shift at $\lambda = 20$ nm is $\sim$10 mm for both the non-shifted and shifted source [solid green and purple lines, respectively, in Figs. 4(b) and 4(c)]. However at $\lambda = 10$ nm the focal shift is $\sim$12 mm [orange curve in Fig. 4(c)], revealing a marked dependence on the wavelength. Also, the HEW completely departs from previously observed behavior [Fig. 4(a)] and is no longer symmetric with respect to its local minimum. Third, the behavior of the HEW as a function of the pointing angle changes as well, since it assumes distinct functional forms at the emission angles $\Delta \vartheta = 0$ μrad and $\Delta \vartheta = -10$ μrad. This preludes to a slippage of HEW minimum as a function of $\Delta \vartheta$. In addition, computations performed at $\Delta \vartheta = +10$ μrad (not shown here) would report a slightly different shape of the HEW, showing that it is by no way symmetric with respect to the nominal propagation axis ($\Delta \vartheta = 0$).

The first effect corresponds to the well known spot size broadening due to shape defects, and it will not be discussed here [a review of independent techniques is given by Raimondi *et al.* (2013)]. The other effects are due to the variation of the wavefront curvature induced by the figure error. In particular, the upstream focal shift is due to the pronounced convexity in the central region of the the vertical residual, which reduces the focusing power of the mirror (a concavity would yield a downstream focal shift). A deeper analysis on the effects of convexity in the central region of the mirror, and of the dependence of the focal planes on the emission angle, will be described in Sections 3.4 and 3.5.

Before exploring this, however, we observe that the distance between the waists of the non-shifted and shifted sources ($\sim$3 mm) appears to be substantially unaltered [arrows in Figs. 4(b) and 4(c)]. This suggests that the source shift and the figure error act independently on the position of the focal plane, and that they can effectively be treated independently by adding a constant term to equation (5). For this reason we will start our numerical investigation by testing the validity of equation (5) in the presence of figure errors.

3.3. Dependence on the source shift

For the inspection of the focal shift we will refer to plots like that of Fig. 6, where we represent the two-dimensional
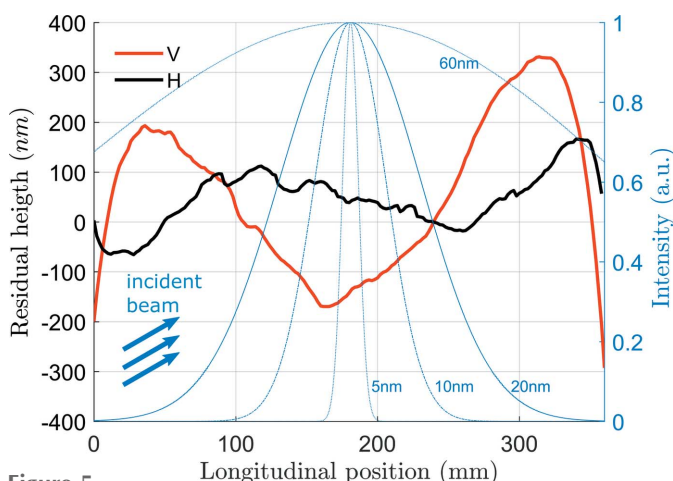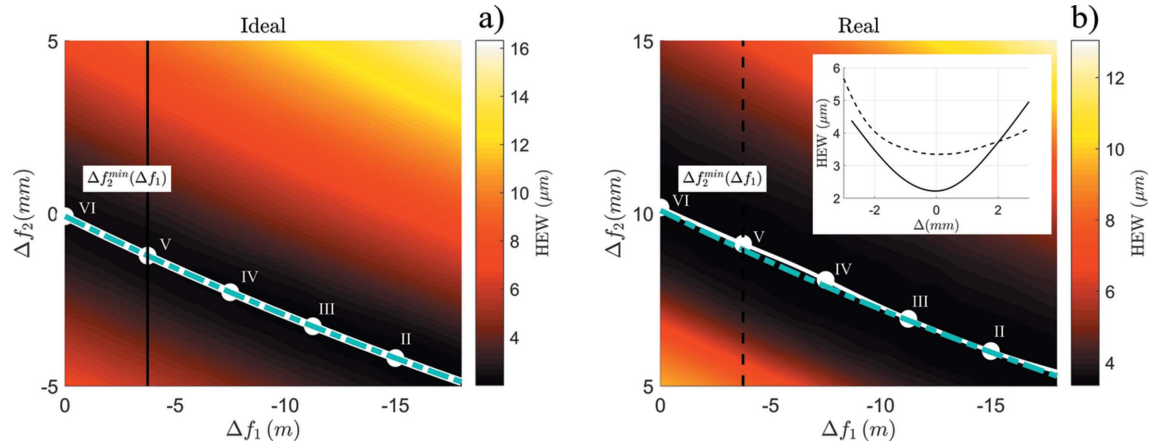
Figure 6
HEW as function of Δf_1 and Δf_2 for the vertical K–B mirror ($\lambda = 20$ nm). (a) Ideal profile. (b) Real profile. Solid white line: interpolating function $\Delta f_2^{min}(\Delta f_1)$. White dots: minima computed for values of Δf_1 corresponding to the position of radiators II–VI. Dashed light blue line: equation (5), computed for continuous values of Δf_1. Inset: profiles of the HEW taken along Δf_2 for $\Delta f_1 = -3.75$ m (corresponding to radiator V). Solid black line: ideal mirror. Dashed black line: real mirror. See description in the text.

distribution of the HEW as a function of the focal shift Δf_2 and of the independent variable (in this case the source shift Δf_1). The color maps the spot size. The locus of points obtained by minimizing the HEW along Δf_2 for any λ (white dots) defines the function $\Delta f_2^{min}(\Delta f_1)$, providing the dependence of the focal shift on the source shift. We report the results for the vertical K–B in the cases of ideal and real surface profiles [Figs. 6(a) and 6(b)]. The solid white curve represents the interpolant function $\Delta f_2^{min}(\Delta f_1)$ passing through the computed minima, while the dashed curve (light blue) corresponds to the theoretical trend of $\Delta f_2^{min}(\Delta f_1)$ for an ideal mirror. Here the minima (white dots) are computed following the spacing of the radiators II–VI (3.75 m).

For an ideal mirror, there is perfect agreement between the numerical computation [$\Delta f_2^{min}(\Delta f_1)$] and the theoretical prediction [$\Delta f_2(\Delta f_1)$] of the focal shift, confirming that the underlying assumptions to equation (4) are satisfied. For the real mirror, in order to match the numerical result, equation (5) can be empirically adapted in the form

$$\Delta f_2(\Delta f_1, \lambda) \simeq m^2 \Delta f_1 + \Delta f_2^{min}(0, \lambda), \qquad (9)$$

where the offset $\Delta f_2^{min}(0, \lambda)$ corresponds to the focal shift at $\Delta f_1 = 0$ for the wavelength λ [e.g. for the vertical K–B, $\Delta f_2^{min}(0, \lambda = 20$ nm$) \simeq 10.25$ mm; $\Delta f_2^{min}(0, \lambda = 10$ nm$) \simeq 12.1$ mm]. The general dependence of the offset $\Delta f_2^{min}(0, \lambda)$ on the wavelength will be investigated in the next section. There is still very close agreement between the corrected theoretical predictions [equation (9)] and the computed results [solid and dashed lines in Fig. 6(b)]. Small deviations are specific to the figure error under consideration and may depend on the illuminated region of the mirror (see next section). Simulations performed at wavelengths in the range 2–80 nm (not shown in this work) confirm that the focal shift due to the source shift and to the figure error can be treated as independent, suggesting that equation (9) is a good approximation for a wide spectral range.

It is worth noting that the distributions of the two HEWs are pretty similar, but in the real case the growth of the HEW

around the locum of minima is slower (i.e. the Rayleigh length is globally longer). The behavior is clear in the inset of Fig. 6(b), which reports the HEW profile taken in correspondence of radiator V (the profiles are shifted so to have the waist in the origin for the sake of comparison). A more dramatic change in the fashion of the 2D-HEW is expected when the wavelength and the source tilt will be considered as free parameters.

3.4. Dependence on the source wavelength

In Fig. 7 we show the distribution of the HEW as a function of the focal shift Δf_2 and of the the wavelength λ. Results for both the vertical and horizontal K–Bs are shown.

At a glance, the two 2D-HEW distributions as well as the computed functions $\Delta f_2^{min}(\lambda)$ largely differ from each other. The horizontal one has a more regular appearance, closer to the theoretical prediction (dashed), whereas the vertical one has a more complex fashion which largely departs from the theory. For the vertical K–B, the focal shift has values around 5–10 mm for λ in the range 10–80 nm [$\Delta f_2(\lambda) \simeq -0.1$ mm nm$^{-1} \times \lambda + 12.5$ nm], whereas for the horizontal K–B the focal shift fluctuates around 0. In both cases, however, the trend of the focal shifts shows an abrupt change for $\lambda \lesssim 5$ nm. Such a behavior can be explained as follows.

Generally speaking, the wavelength determines the interference effects and the extension of the illuminated mirror area [the latter by virtue of equation (8)]. Whereas the effects due the interference cannot be intuitively described, since they rely on the solution of the Huygens–Fresnel integral, the effects due to the beam footprint offer a simpler understanding. In the case of a beam with a very narrow footprint, the impinging wavefront is sensitive to localized curvature defects. These ones may easily induce a large curvature variation over the transverse beam size, thus producing a pronounced focal shift. Conversely, in the presence of a large beam footprint, the overall effect on the wavefront is milder. The reason is that the phase variations due to defects at the
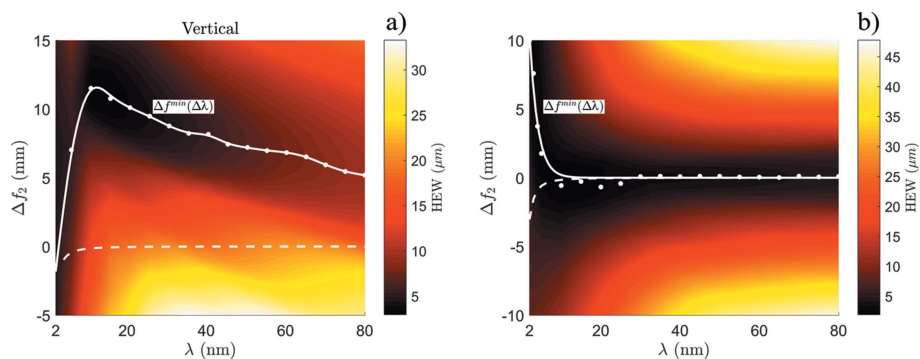
Figure 7
HEW as a function of Δf_2 and λ for vertical and horizontal K–B. Dots: computed minima for each sample of λ. Solid line: interpolating function $\Delta f_2^{min}(\lambda)$. Dashed line: equation (5) as a function of λ for $\Delta f_1 = 0$ [same as in Fig. 3(a)]. The discrepancy between theory and simulations is due to figure errors, which induce different trends in the vertical and horizontal K–Bs.

small scales appear as fast fluctuations over the slower phase error due to the larger spatial scale. It follows that, by integrating over a large area (due to the extended beam footprint), the fast contributions partially compensate, so that it is likely to obtain a less pronounced focal shift than the previous case.

Clearly, the magnitude of the effect depends on the figure error under consideration, and so it is case-specific. As far as the focused spot size is concerned, the behavior is reversed. Large beam footprints (*i.e.* large wavelengths) are more prone to emphasize the phase errors derived from an extended integration area, thus resulting into larger values of the HEW. On the other hand, smaller beam footprints (*i.e.* smaller wavelengths) are more likely to suppress such phase errors, yielding smaller values of the HEW. For example, the focal shift and the HEW for the spot focused by the vertical K–B are $\Delta f_2 \simeq +11.5$ mm and HEW $\simeq 4$ μm at $\lambda = 10$ nm, and $\Delta f_2 \simeq +5$ mm and HEW $\simeq 11$ μm at $\lambda = 80$ nm. Larger values of the HEW at larger wavelengths are also due to edge diffraction that becomes increasingly important. For $\lambda \lesssim 5$ nm the direction of the focal shift is reversed, probably due to the fact that the beam footprint sweeps through the minimum in the residual height (at 160 mm). This fact shall be ascribed to the particularities of the figure error under examination. The horizontal K–B, for instance, yields a different trend of the focal shift in the same spectral range. It is worth noticing that, for both K–Bs, such a dependence at $\lambda \lesssim 5$ nm is so strong that it overrides the Gaussianity effects, *i.e.* the focal displacement induced by the figure error is always greater than that induced by the finite-source size.

3.5. Dependence on the source pointing angle

We can apply a similar reasoning to the pointing angle of the source ($\Delta\vartheta$). Since the focal shift has a strong dependence on the wavelength, it is appropriate to test the HEW for different values of λ ($\lambda = 20$ nm, $\lambda = 10$ nm and $\lambda = 5$ nm). The results are shown in Fig. 8 for values of $\Delta\vartheta$ in the range (-30 μrad, $+15$ μrad). At short wavelengths (*i.e.* for small beam footprints) the distribution of the HEW and

its corresponding function $\Delta f_2^{min}(\Delta\vartheta)$ exhibit fine details over the small angular size, appearing peaked and fast varying, whereas at long wavelengths (*i.e.* for large beam footprints) their appearance is broader and smoother. The fine-structure of $\Delta f_2^{min}(\Delta\vartheta)$ is related to the short- and middle-scale contributions of the figure error, as it is visible by comparing Figs. 8(e), 8(f) and Fig. 5. The two peaks of Fig. 8(e) recall those of the vertical residual in Fig. 5, and the wavy details in the central region in Fig. 8(f) recall that of the horizontal residual in the central region of the mirror. The knowledge of $\Delta f_2^{min}(\Delta\vartheta)$ is useful in two circumstances: to identify the best incidence angle on the mirror surface and to predict the average focal shift due to the angular jitter.

3.5.1. Best incidence angle. From Figs. 8(a), 8(c) and 8(e) (green crosses) it can be seen that smaller values of the HEW are achieved for negative values of $\Delta\vartheta$, *i.e.* for larger incidence angles than the nominal one (corresponding to $\Delta\vartheta = 0$). This suggests operating the photon beam at an effective incidence angle $\tilde{\vartheta}_i = \vartheta_i + \Delta\tilde{\vartheta}$, where the work point $\Delta\tilde{\vartheta}$ should be chosen by minimizing the value of the HEW. Practically, if the HEW is slowly varying around its minimum, it is reasonable to choose $\Delta\tilde{\vartheta}$ to be the smallest possible, in order to stick to the nominal design. Since the emission angle of the source is a consequence of the machine optimization, it cannot be easily modified. For this purpose, plane mirrors or other deflecting optical elements are typically used to correct the beam trajectory. In principle, in order to reproduce a deflection $\Delta\vartheta$ of the source by means of N deflecting mirrors, each deflection angle $\Delta\vartheta_k$ can be independently adjusted provided that the relation $\sum_{k=1}^{N} \Delta\vartheta_k = \Delta\vartheta/2$ is satisfied. It shall be kept in mind, however, that the impact region of the beam on the focusing mirror will generally change if the lateral positions of the deflectors are not properly adjusted (Fig. 9). For this reason, two computations with distinct numbers of deflecting elements will not in general yield the same result, even if the aforementioned condition on the angles is met. Practically, however, the alignment of an X-ray focusing system is a complex operation that is periodically achieved in beam tuning operations, with the aid of techniques that allow a fast and quantitative response (such as wavefront sensing). In such a perspective, the information provided by simulating a single source tilt, as in Fig. 8, represents a valuable support, although not simulating the exact layout of the transport system. For making this approximation more effective, it shall be kept in mind that the pointing variation of the source is better mimed by changing the pointing of most upstream deflectors, rather than of the downstream ones.

3.5.2. Angular jitter. The angular jitter is the shot-to-shot fluctuation of the photon beam around its mean direction of propagation (at FERMI $\simeq 5$ μrad r.m.s.). It is a direct conse-
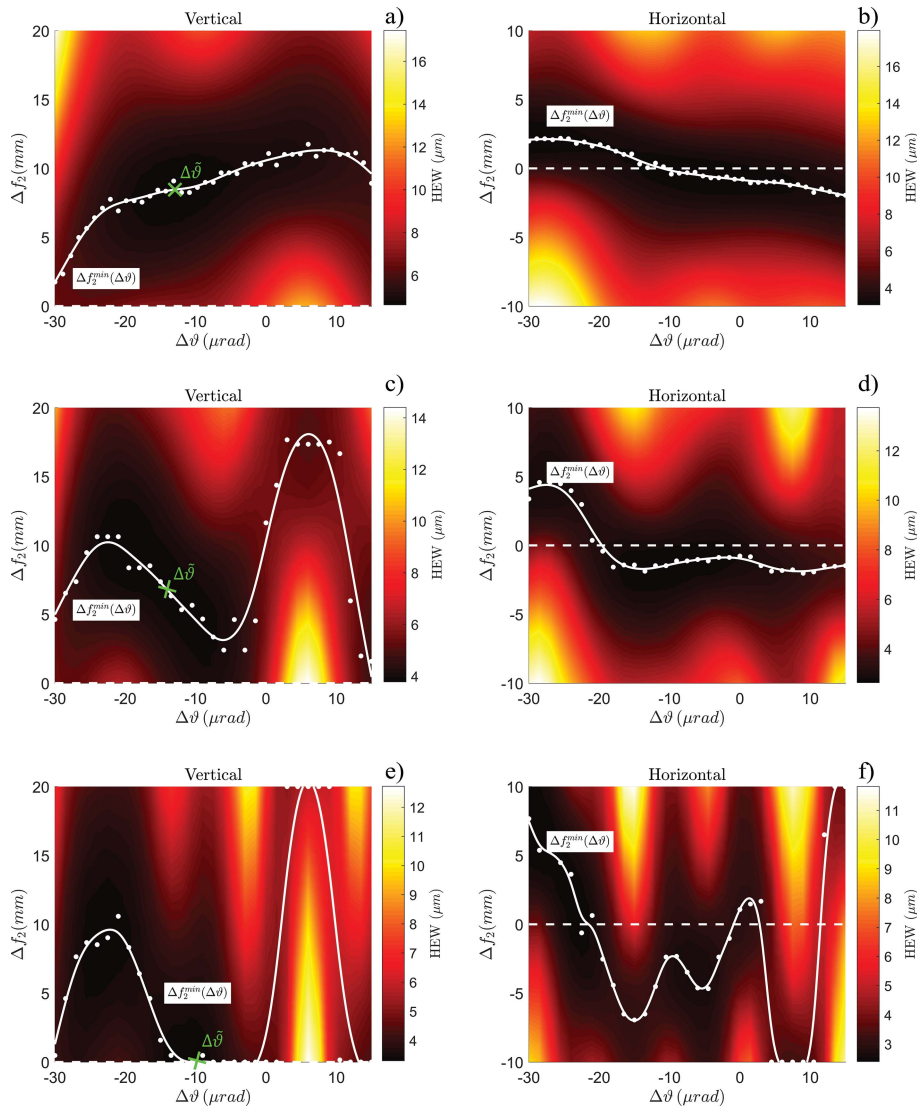
Figure 8
HEW as a function of Δf_2 and $\Delta \vartheta$ for K–B mirrors. (a, b) $\lambda = 20$ nm. (c, d) $\lambda = 10$ nm. (e, f) $\lambda = 5$ nm. Dots: computed minima for each sample of $\Delta \vartheta$. Solid lines: interpolating function $\Delta f_2^{min}(\Delta \vartheta)$. Dashed lines: theory.
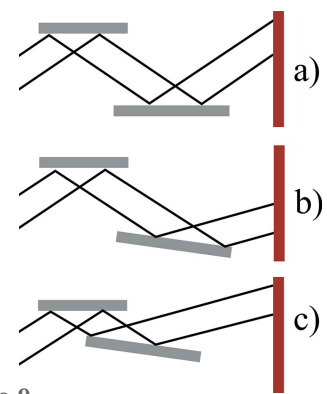

Figure 9
(a) Initial alignment. (b) Pitched mirror (new exit angle and transverse position). (c) Pitched and shifted mirror (new exit angle, same transverse position).

with. So, for instance, the latter aforementioned case would induce a negligible effect in diffraction experiments, since the HEW is very small. Conversely, it would induce a blatant effect in beam metrology applications, where the position of the focal plane effectively matters.

As far as the wavelength dependence is concerned, since the function $\Delta f_{2,\lambda}^{min}(\Delta \vartheta)$ appears to be progressively fast varying at short wavelengths, in this spectral range the angular jitter is expected to yield a greater effect (Δf_2 of the order of a few millimetres for $\lambda = 10$ nm and an angular jitter of 5 µrad r.m.s.).

quence of electron orbit fluctuations and, unlike the neat change of the emission angle, it cannot be compensated by means of static deflection optics. The angular jitter induces a focal shift (Fig 8) that depends on the figure error and the wavelength involved. Depending on the functional form of Δf_2^{min}, the fluctuations of the focal shift may also be strongly dependent on the selected work angle $\Delta \tilde{\vartheta}$. So, the choice of $\Delta \tilde{\vartheta}$ is important not only for achieving a tight focusing but also for properly minimizing the focal plane fluctuations. For instance, an r.m.s. fluctuation of ∼5 µrad at $\lambda = 10$ nm [Fig. 8(c)] would yield a ∼12 mm focal shift and a 20% HEW variation if taken around $\Delta \vartheta = 0$ µrad (nominal work angle), whereas the same fluctuation would yield a ∼5 mm focal shift and a <5% HEW variation if taken around $\Delta \vartheta = 0$ µrad (optimized work angle). It shall be pointed out that, for many experimental applications, the fluctuations of the HEW do matter more than the fluctuation of Δf_2 they are associated

4. Conclusions

We have addressed the focusing of a Gaussian beam through an elliptical mirror, studying for the first time the focal shift induced by the source displacements and the optical figure errors. The aim was to disentangle the two contributions at advanced light sources, such as FELs. Knowledge of the focal shift is important whenever critical properties of the light source, such as longitudinal position, wavelength and pointing angle, are subject to change or are possibly unknown. This becomes especially relevant when the requirements on the performance of the focusing optics are highly demanding.

We have derived the focal shift for an ideal mirror [equation (2)], starting from the corrected lens-maker equation for a Gaussian beam and approximating the elliptical arc section of focal lengths f_1, f_2 to a parabolic section of focal length $1/f = 1/f_1 + 1/f_2$ [equation (5)]. The relation is valid for any spectral range, it holds for conventional point-like sources and can be extended to non-Gaussian beams by introducing the propagation factor M^2. Furthermore, we have extended the study to the case of a real mirror affected by measured

figure errors. We have considered a set of K–B mirrors operating in the XUV bandwidth at the seeded FEL FERMI (Trieste, Italy). Simulations were performed in the 2–80 nm wavelength range with a Gaussian beam of size $w_0 = 180$ µm (compatible with FERMI characteristics). The focal shift as a function of the wavelength λ and of the source pointing angle $\Delta\vartheta$ has been numerically investigated. We observe that the presence of figure errors substantially affects the dependence of the focal shift on λ and $\Delta\vartheta$, inducing a deviation from the theoretical predictions. For the vertical K–B, we computed a neat shift of 5–11 mm in the spectral range 10 nm < λ < 80 nm, whereas a negligible shift is induced by the horizontal mirror. The differences are ascribed to the figure error, which is smaller in the latter case. The pointing-related dependence of the focal shift is strongly dependent on the wavelength as well. For instance, a variation of $\Delta\vartheta \simeq \pm 5$ µrad around the nominal pointing direction yields a shift of ~ 1.5 mm at $\lambda = 10$ nm and a shift of ~ 11 mm at $\lambda = 5$ nm.

The results presented in this paper identify different contributions to the focal shift, which can be due to either a genuine source shift or to the effects of the figure error on the wavelength and pointing instabilities. The disentanglement of these contributions opens the way to a manifold of applications, including: predicting focal spot changes at the endstation, optimizing the alignment of the optics and improving source metrology. This is especially true when evaluating the fluctuations of the source position, as the angular jitter can be mistaken with a source jitter. Such an effect is expected to become even more critical at SASE-FEL sources, where the angular jitter is inherently larger than that in a seeded FEL because of the longer path that electrons have to cover to reach saturation in the light emission.

The approach developed in this work can be profitably applied to the study of hard X-ray mirrors, which are characterized by much lower r.m.s. figure errors (<10 nrad) and outstanding focusing performance. At hard X-ray wavelengths, the scattering from surface roughness is not negligible and it largely contributes to the HEW of the focal spot. However, due to its stochastic nature, the roughness should not affect the longitudinal position of the focal plane. Nonetheless, this prediction should be validated with dedicated numerical simulations. In this regard, the Database for Metrology (DABAM) provides a valuable source for the reader that may be interested in extending the scope of this work at X-ray wavelengths.

References

Abadi, M. M., Ghassemlooy, Z., Smith, D. & Ng, W. P. (2015). *J Electr. Comput. Eng. Innov.* **3**, 1–11.

Allaria, E., Appio, R., Badano, L., Barletta, W., Bassanese, S., Biedron, S., Borga, A., Busetto, E., Castronovo, D., Cinquegrana, P., Cleva, S., Cocco, D., Cornacchia, M., Craievich, P., Cudin, I., D'Auria, G., Dal Forno, M., Danailov, M., De Monte, R., De Ninno, G., Delgiusto, P., Demidovich, A., Di Mitri, S., Diviacco, B., Fabris, A., Fabris, R., Fawley, W., Ferianis, M., Ferrari, E., Ferry, S., Froehlich, L., Furlan, P., Gaio, G., Gelmetti, F., Giannessi, L., Giannini, M., Gobessi, R., Ivanov, R., Karantzoulis, E., Lonza, M., Lutman, A., Mahieu, B., Milloch, M., Milton, S., Musardo, M., Nikolov, I., Noe, S., Parmigiani, F., Penco, G., Petronio, M., Pivetta, L., Predonzani, M., Rossi, F., Rumiz, L., Salom, A., Scafuri, C., Serpico, C., Sigalotti, P., Spampinati, S., Spezzani, C., Svandrlik, M., Svetina, C., Tazzari, S., Trovo, M., Umer, R., Vascotto, A., Veronese, M., Visintini, R., Zaccaria, M., Zangrando, D. & Zangrando, M. (2012). *Nat. Photon.* **6**, 699–704.

Allaria, E., Badano, L., Bassanese, S., Capotondi, F., Castronovo, D., Cinquegrana, P., Danailov, M. B., D'Auria, G., Demidovich, A., De Monte, R., De Ninno, G., Di Mitri, S., Diviacco, B., Fawley, W. M., Ferianis, M., Ferrari, E., Gaio, G., Gauthier, D., Giannessi, L., Iazzourene, F., Kurdi, G., Mahne, N., Nikolov, I., Parmigiani, F., Penco, G., Raimondi, L., Rebernik, P., Rossi, F., Roussel, E., Scafuri, C., Serpico, C., Sigalotti, P., Spezzani, C., Svandrlik, M., Svetina, C., Trovó, M., Veronese, M., Zangrando, D. & Zangrando, M. (2015). *J. Synchrotron Rad.* **22**, 485–491.

Allaria, E., Bencivenga, F., Borghes, R., Capotondi, F., Castronovo, D., Charalambous, P., Cinquegrana, P., Danailov, M. B., De Ninno, G., Demidovich, A., Di Mitri, S., Diviacco, B., Fausti, D., Fawley, W. M., Ferrari, E., Froehlich, L., Gauthier, D., Gessini, A., Giannessi, L., Ivanov, R., Kiskinova, M., Kurdi, G., Mahieu, B., Mahne, N., Nikolov, I., Masciovecchio, C., Pedersoli, E., Penco, G., Raimondi, L., Serpico, C., Sigalotti, P., Spampinati, S., Spezzani, C., Svetina, C., Trovò, M. & Zangrando, M. (2013). *Nat. Commun.* **4**, 2476.

Allaria, E., Diviacco, B., Callegari, C., Finetti, P., Mahieu, B., Viefhaus, J., Zangrando, M., De Ninno, G., Lambert, G., Ferrari, E., Buck, J., Ilchen, M., Vodungbo, B., Mahne, N., Svetina, C., Spezzani, C., Di Mitri, S., Penco, G., Trovó, M., Fawley, W. M., Rebernik, P. R., Gauthier, D., Grazioli, C., Coreno, M., Ressel, B., Kivimäki, A., Mazza, T., Glaser, L., Scholz, F., Seltmann, J., Gessler, P., Grünert, J., De Fanis, A., Meyer, M., Knie, A., Moeller, S. P., Raimondi, L., Capotondi, F., Pedersoli, E., Plekan, O., Danailov, M. B., Demidovich, A., Nikolov, I., Abrami, A., Gautier, J., Lüning, J., Zeitoun, P. & Giannessi, L. (2014). *Phys. Rev. X*, **4**, 041040.

Aschenbach, B. (2005). *Proc. SPIE*, **5900**, 59000D.

Bachelard, R., Mercère, P., Idir, M., Couprie, M. E., Labat, M., Chubar, O., Lambert, G., Zeitoun, P., Kimura, H., Ohashi, H., Higashiya, A., Yabashi, M., Nagasono, M., Hara, T. & Ishikawa, T. (2011). *Phys. Rev. Lett.* **106**, 1–4.

Capotondi, F., Pedersoli, E., Bencivenga, F., Manfredda, M., Mahne, N., Raimondi, L., Svetina, C., Zangrando, M., Demidovich, A., Nikolov, I., Danailov, M., Masciovecchio, C. & Kiskinova, M. (2015). *J. Synchrotron Rad.* **22**, 544–552.

Chu, T. (2004). *IEEE Trans. Antennas Propagat.* **31**, 614–619.

Citterio, O. & O'Dell, S. L. (2004). *Proc. SPIE*, **5168**, 1–532.

Doyuran, A., Babzien, M., Shaftan, T., Yu, L. H., DiMauro, L. F., Ben-Zvi, I., Biedron, S. G., Graves, W., Johnson, E., Krinsky, S., Malone, R., Pogorelsky, I., Skaritka, J., Rakowsky, G., Wang, X. J., Woodle, M., Yakimenko, V., Jagger, J., Sajaev, V. & Vasserman, I. (2001). *Phys. Rev. Lett.* **86**, 5902–5905.

Ferrari, E., Allaria, E., Buck, J., De Ninno, G., Diviacco, B., Gauthier, D., Giannessi, L., Glaser, L., Huang, Z., Ilchen, M., Lambert, G., Lutman, A. A., Mahieu, B., Penco, G., Spezzani, C. & Viefhaus, J. (2015). *Sci. Rep.* **5**, 13531.

Ferrari, E., Spezzani, C., Fortuna, F., Delaunay, R., Vidal, F., Nikolov, I., Cinquegrana, P., Diviacco, B., Gauthier, D., Penco, G., Ribič, P. R., Roussel, E., Trovò, M., Moussy, J.-B., Pincelli, T., Lounis, L., Manfredda, M., Pedersoli, E., Capotondi, F., Svetina, C., Mahne, N., Zangrando, M., Raimondi, L., Demidovich, A., Giannessi, L., De Ninno, G., Danailov, M. B., Allaria, E. & Sacchi, M. (2016). *Nat. Commun.* **7**, 10343.

Gangopadhyay, S. & Sarkar, S. (1997). *Appl. Opt.* **36**, 8582–8586.

Goldsmith, P. F. (1998). *Quasioptical Systems: Gaussian Beam Quasioptical Propogation and Applications.* Wiley-IEEE Press.

Hara, T., Inubushi, Y., Katayama, T., Sato, T., Tanaka, H., Tanaka, T., Togashi, T., Togawa, K., Tono, K., Yabashi, M. & Ishikawa, T. (2013). *Nat. Commun.* **4**, 2919.

Kayser, Y., Rutishauser, S., Katayama, T., Kameshima, T., Ohashi, H., Flechsig, U., Yabashi, M. & David, C. (2016). *Opt. Lett.* **41**, 733–736.

Kim, K.-J., Huang, Z. & Lindberg, R. (2017). *Synchrotron Radiation and Free-Electron Lasers.* Cambridge University Press.

Liu, Y., Seaberg, M., Zhu, D., Krzywinski, J., Seiboth, F., Hardin, C., Cocco, D., Aquila, A., Nagler, B., Lee, H. J., Boutet, S., Feng, Y., Ding, Y., Marcus, G. & Sakdinawat, A. (2018). *Optica*, **5**, 967.

Lutman, A. A., Maxwell, T. J., MacArthur, J. P., Guetg, M. W., Berrah, N., Coffee, R. N., Ding, Y., Huang, Z., Marinelli, A., Moeller, S. & Zemella, J. C. U. (2016). *Nat. Photon.* **10**, 745–750.

Manfredda, M. & Raimondi, L. (2018). *WISEr*, https://www.aps.anl.gov/Science/Scientific Software/OASYS.

Massey, G. A. & Siegman, A. E. (1969). *Appl. Opt.* **8**, 975–978.

Nightingale, C. R. (1993). *Telecommunications Engineer's Reference Book*, edited by F. Mazda, ch. 24. Amsterdam: Elsevier.

Nistea, I. T., Alcock, S. G., Kristiansen, P. & Young, A. (2017). *J. Synchrotron Rad.* **24**, 615–621.

O'Dell, S. L., Elsner, R. F., Kolodziejczak, J. J., Weisskopf, M. C., Hughes, J. P. & Van Speybroeck, L. P. (1993). *Proc. SPIE*, **1742**, 171.

Peatman, W. B. (1997). *Gratings, Mirrors and Slits: Beamline Design for Soft X-ray Synchrotron Radiation Sources.* Amsterdam: Gordon & Breach.

Pedersoli, E., Capotondi, F., Cocco, D., Zangrando, M., Kaulich, B., Menk, R. H., Locatelli, A., Mentes, T. O., Spezzani, C., Sandrin, G., Bacescu, D. M., Kiskinova, M., Bajt, S., Barthelmess, M., Barty, A., Schulz, J., Gumprecht, L., Chapman, H. N., Nelson, A. J., Frank, M., Pivovaroff, M. J., Woods, B. W., Bogan, M. J. & Hajdu, J. (2011). *Rev. Sci. Instrum.* **82**, 043711.

Prazeres, R., Ortega, J. M., Bazin, C., Bergher, M., Billardon, M., Couprie, M. E., Velghe, M. & Petroff, Y. (1988). *Nucl. Instrum. Methods Phys. Res. A*, **272**, 68–72.

Prince, K. C., Allaria, E., Callegari, C., Cucini, R., De Ninno, G., Di Mitri, S., Diviacco, B., Ferrari, E., Finetti, P., Gauthier, D., Giannessi, L., Mahne, N., Penco, G., Plekan, O., Raimondi, L., Rebernik, P., Roussel, E., Svetina, C., Trovò, M., Zangrando, M., Negro, M., Carpeggiani, P., Reduzzi, M., Sansone, G., Grum-Grzhimailo, A. N., Gryzlova, E. V., Strakhova, S. I., Bartschat, K., Douguet, N., Venzke, J., Iablonskyi, D., Kumagai, Y., Takanashi, T., Ueda, K., Fischer, A., Coreno, M., Stienkemeier, F., Ovcharenko, Y., Mazza, T. & Meyer, M. (2016). *Nat. Photon.* **10**, 176–179.

Raimondi, L., Manfredda, M., Mahne, N., Cocco, D., Capotondi, F., Pedersoli, E., Kiskinova, M. & Zngrando, M. (2019). *J. Synchrotron Rad.* **26**, 1462–1472.

Raimondi, L. & Spiga, D. (2015). *Astron. Astrophys.* **573**, A22.

Raimondi, L., Svetina, C., Mahne, N., Cocco, D., Abrami, A., De Marco, M., Fava, C., Gerusina, S., Gobessi, R., Capotondi, F., Pedersoli, E., Kiskinova, M., De Ninno, G., Zeitoun, P., Dovillaire, G., Lambert, G., Boutu, W., Merdji, H., Gonzalez, A. I., Gauthier, D. & Zangrando, M. (2013). *Nucl. Instrum. Methods Phys. Res. A*, **710**, 131–138.

Sanchez del Rio, M. & Rebuffi, L. (2019). *AIP Conf. Proc.* **2054**, 060081.

Self, S. A. (1983). *Appl. Opt.* **22**, 658–661.

Siegman, A. E. (1998). *Proceedings DPSS (Diode Pumped Solid State) Lasers: Applications and Issues*, 1 January 1998, Washington, DC, USA. MQ1.

Siegman, A. E. & Weichel, H. (1974). *Am. J. Phys.* **42**, 521–523.

Signorato, R. (1999). *Proc. SPIE*, **3773**, 50.

Svetina, C., Grazioli, C., Mahne, N., Raimondi, L., Fava, C., Zangrando, M., Gerusina, S., Alagia, M., Avaldi, L., Cautero, G., de Simone, M., Devetta, M., Di Fraia, M., Drabbels, M., Feyer, V., Finetti, P., Katzy, R., Kivimäki, A., Lyamayev, V., Mazza, T., Moise, A., Möller, T., O'Keeffe, P., Ovcharenko, Y., Piseri, P., Plekan, O., Prince, K. C., Sergo, R., Stienkemeier, F., Stranges, S., Coreno, M. & Callegari, C. (2015). *J. Synchrotron Rad.* **22**, 538–543.

Takacs, P. Z. (1986). *Nucl. Instrum. Methods Phys. Res. A*, **246**, 227–241.

Willingale, R. (1988). *Appl. Opt.* **27**, 1423–1429.

Yu, Y. & Dou, W. (2010). *9th International Symposium on Antennas, Propagation and EM Theory (ISAPE 2010)*, 29 November–2 December 2010, Guangzhou, China, pp. 636–638.